



# Electrodeposition of ZnO nanorods on graphene: tuning the topography for application as tin oxide-free electron transport layer

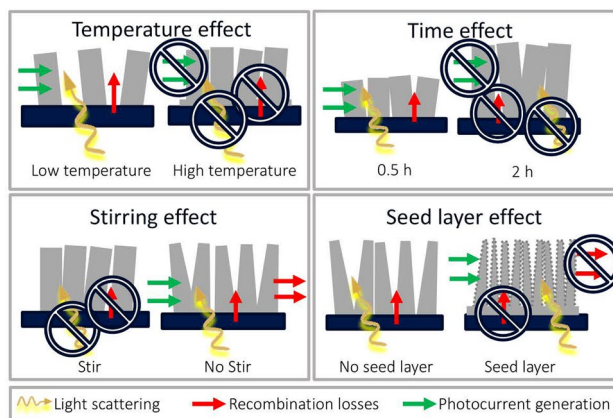
Claudia C. Villarreal<sup>1,3</sup> · Danish Pirzada<sup>2</sup> · Annie Wong<sup>2</sup> · Ashok Mulchandani<sup>1,2,4</sup>

Received: 24 October 2020 / Accepted: 18 January 2021 / Published online: 28 April 2021  
© The Author(s), under exclusive licence to Springer Nature B.V. 2021

## Abstract

The heterostructure of graphene and ZnO nanorods is attractive as a tin oxide-free electron transport layer for a broad variety of excitonic photovoltaic technologies. This work focuses on the effect of electrodeposition variables on morphology and performance of vertically aligned zinc oxide nanorods (ZVNRs) on graphene. This in situ growth technique has potential for fabrication of a wide variety of graphene heterostructures under mild synthesis conditions to prevent graphene damage. Large area graphene was grown by chemical vapor deposition, stacked up to four atomic layers, and transferred to glass. ZVNRs were electrodeposited on the graphene-coated glass and the topography was controlled by changing the electrodeposition parameters of the time, temperature, stirring, and seeding layers. The mechanisms controlling the cathodic electrodeposition of nanocrystals on graphene were studied by scanning electron microscopy of the ZVNRs topography. The effect of the topography of the ZVNRs on the electron generation and transport was studied for photoanode application in reference dye-sensitized solar cells. The charge transfer resistance and kinetics of the materials as photoanodes were measured with the techniques of linear sweep voltammetry, open circuit voltage decay, and electrochemical impedance spectroscopy. The optimization of ZnO growth resulted in an increase of the surface-to-volume ratio of the electrode from 10 to 250 mm<sup>-1</sup>, 60-fold increase of electron lifetime and ten-fold increase in power output. The results of this study provide fundamental understanding for designing electrodeposition processes of the hybrid ZVNR/graphene material.

## Graphic abstract



**Keywords** Graphene heterostructure · Electron transport layer · Cathodic electrodeposition · Tin oxide-free · Vertically aligned ZnO nanorods

✉ Claudia C. Villarreal  
cchaves@itcr.ac.cr

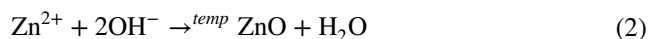
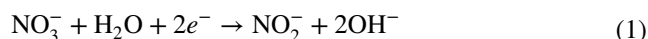
Extended author information available on the last page of the article

## 1 Introduction

A photoelectrochemical cell is a device that harvests sunlight to convert it into other forms of energy such as chemical or electrical and is based on a photoanode connected to a counter-electrode via an electrolyte. The photoanode absorbs the photons and drives oxidation reactions of a mediator in the electrolyte, which are regenerated in the counter-electrode. Nanostructured wide-bandgap semiconductors, like TiO<sub>2</sub> or ZnO, spread over a transparent conductor are attractive as photoanodes due to their low cost and wide availability. The limited solar spectrum range that ZnO or TiO<sub>2</sub> absorbs in the ultraviolet portion of the sun spectrum is expanded to visible range by sensitizing the photoanodes with photoactive materials, such as organic and metalorganic dyes [1] quantum dots [2], plasmonic nanoparticles [3], perovskites [4, 5], and photosynthetic biomolecules [6, 7]. A large portion of the photoanode cost corresponds to the choice of transparent conductor, typically doped tin oxide. Tin oxides are fragile materials derived from non-abundant sources, like cassiterite, which classifies as conflict mineral and can adversely affect both water quality, human health and social conditions [8–10]. Graphene is a sustainable alternative to tin oxides, as it can be obtained from a variety of organic sources, including waste byproducts, as illustrated in Fig. 1. Pristine CVD-graphene with large domain size stands out as the most promising graphene variant for TC application, not only due to its superior optoelectronic properties, but also because large area films can be produced at an industrial scale [11].

ZnO and TiO<sub>2</sub> are the two most common wide-bandgap semiconductors for photoanodes with very similar bandgaps; however ZnO has an electron mobility that is two to three orders of magnitude larger [12]. Additionally, ZnO is also more reactive and it can be synthesized into its crystalline form under mild conditions with a variety of shapes, being more compatible for in situ growth on graphene, considering the high oxidation susceptibility of the latter. The vertically aligned ZnO nanorods (ZVNRs) offer a large surface area for light scattering and absorption. Their short radial distance promotes rapid transport of minority charge carriers towards the junction for exciton separation, they have lower electron transfer resistance through the semiconductor in comparison to nanoparticles assemblies where electrons must cross several interfaces with high probability of recombination [13–15]. The ZVNR/graphene heterostructure (ZVNR/G) has been reported recently as an electron transport layer in perovskite solar cells with efficiency of 12.87% for pristine graphene and 16.82% for nitrogen-doped graphene [16]. Therefore, understanding how the parameters for ZVNR in situ growth on graphene affect its topography and photoanode performance is fundamental for the future development of low-cost, sustainable photoelectrochemical cells.

Electrodeposition of nanostructured thin films has been gaining attention lately due to the high-end quality of the film, the excellent process control and its advantages over other techniques like doctor-blade and chemical vapor deposition [17]. Crystalline nanostructures can be obtained with electrodeposition at temperatures below 100 °C without further need for thermal treatments, which is a critical requirement for the development of flexible devices on polymeric substrates. This technique is an in situ deposition method, which results in reduced interfacial resistance. It is also facile and low-cost, as no expensive facilities or high energy processes are required. Cathodic deposition of transparent ZnO films on conductive glasses from a simple aqueous Zn(NO<sub>3</sub>)<sub>2</sub> electrolyte was first reported in 1996 by Ozaki and Omi, with films showing (0001) preferred orientation under certain conditions [18]. A systemic study of the electrodeposition of ZVNRs on tin oxide substrate using nitrate ion as a precursor was first reported in 2012 [19]. The reaction leading to oxide formation is the electrogeneration of a base (Eq. 1) followed by dehydration (Eq. 2) as described in Eqs. 1 and 2:



In a photoanode, the power conversion efficiency is strongly dependent on the semiconductor surface area since it determines the junction area at which the photoelectrochemical reactions take place. For an array of ZVNRs, the surface area can be increased by reducing the diameter of the rods and increasing their length. Several approaches are used to reduce the diameter of ZVNRs, one of the most effective being the use of seed layer, also called buffer layer. This seed layer provides a dense source of nucleation centers for the growth of the ZVNRs [20].

Graphene variants like reduced graphene oxide [21], oxidized CVD-graphene [22], pristine CVD-graphene [23], and graphene foam [24] have been studied as conductive substrates for the fabrication of the ZVNR/G by electrodeposition. The mild growth conditions of electrodeposition prevent graphene damage by oxidation. A negative bias applied seems to protect graphene from defect introduction, as it has been observed in electrochemical delamination from metallic foils [25]. We have demonstrated that cathodic electrodeposition on graphene offers a feasible in situ route to fabricate the ZVNR/G hybrid, while preserving the sp<sup>2</sup> structure of graphene. The ZVNR growth conditions on graphene have been optimized to obtain continuous carpet of crystalline vertically aligned nanorods highly texturized in the [0001] direction. The graphene substrate has been observed to induce mosaicity

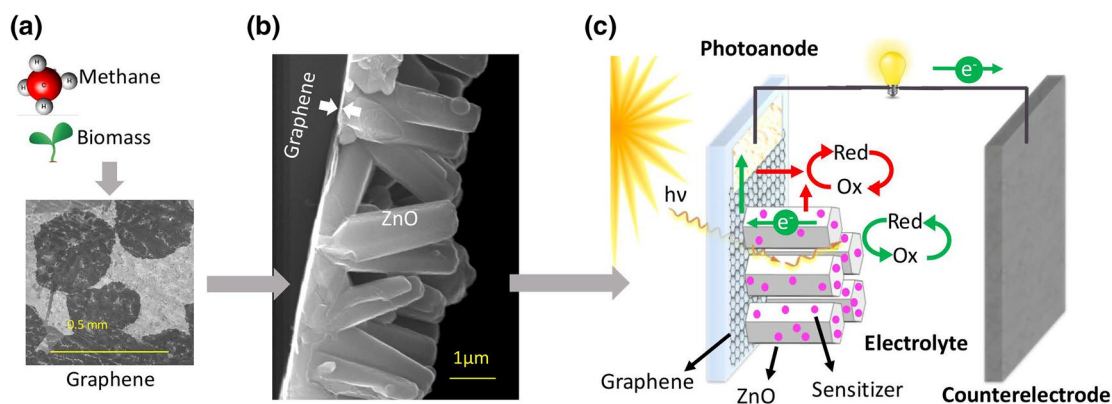


**Fig. 1** Sustainable fabrication of tin-oxide free photoanode. **a** Synthesis of high-quality graphene, a carbon-based transparent conductor produced from abundant renewable resources. **b** Electrodeposition of ZnO nanostructures on graphene to make a hybrid photoanode. **c**

and crystal distortions that could be attributed to misfit dislocations in the ZVNRs, due to the lattice mismatch between graphene and ZnO that generates an out-of-plane strain [26].

In this work, we explore the effects of electrodeposition parameters on the ZVNR morphology and the performance of the hybrid as a photoanode in a DSC. The electrodeposition parameters investigated were temperature, time, stirring, and the use of a seeding layer. The photoelectron generation and transport in the ZVNR/G was studied via linear sweep voltammetry (LSV), open circuit voltage decay (OCVD), and electrochemical impedance spectroscopy (EIS). This study aims to explore the fundamentals of crystal growth in graphene as a sustainable conductive substrate and elucidate the predominant mechanisms of power generation and loss of the heterostructure in solar energy harvesting application.

## 2 Methods

### 2.1 Graphene transparent conductive layer

A continuous graphene film was grown on Cu foil using ambient-pressure CVD to yield a domain size up to 300 μm. A Cu foil is annealed for two hours at 1030 °C in the furnace at atmospheric pressure with Ar (300 sccm) and H<sub>2</sub> (15 sccm). Then, graphene is grown with 375 sccm of diluted methane in Ar (90 ppm) and 15 sccm of H<sub>2</sub> for 60 min and cooled with Ar (300 sccm) and H<sub>2</sub> (15 sccm). More details are provided in Supporting Information (SI) [26, 27]. The graphene on copper was spin-coated on one side with PMMA. The copper was etched in 0.3 M FeCl<sub>3</sub> and cleaned with DI water. The floating graphene/PMMA film was stacked onto a second graphene/Cu film. The

Use of ZVNR/G hybrid as a photoanode, electron transfer processes occurring: arrows in green indicate power generating processes, arrows in red indicate power loss processes

etching and stacking processes were repeated until 4-layered graphene (4LG) was obtained. The 4LG was then transferred onto a clean glass substrate, with the graphene in contact with the glass. The PMMA was dissolved in acetone, the graphene annealed in Ar/H<sub>2</sub> at 250 °C, and 10/120 nm Cr/Au contacts were e-beam evaporated.

### 2.2 Electrodeposition of ZVNR and pre-deposition of seeding layer on graphene

The ZVNR electrodeposition and pre-deposition of seeding layer on graphene was performed using a CHI 660C electrochemical station and CHI6005E electrochemical workstation software.

For the ZVNR electrodeposition, a three-electrode configuration was used, with graphene-on-glass as the working electrode, platinum mesh as the counter-electrode, and Ag/AgCl<sub>sat'd</sub> as the reference electrode. PMMA was used as dielectric coating on the Cr/Au contact. For the ZVNR growth, a cathodic potential was applied to the graphene in 10 mM Zn(NO<sub>3</sub>)<sub>2</sub> aqueous solution to maintain a current density of 0.4 mA cm<sup>-2</sup>, which had been optimized in our previous report to obtain well-aligned crystalline ZVNRs on graphene [25]. We studied the effect of three growth variables: temperature, time and stirring. The temperature studied varied between 70 and 80 °C, the time was varied from 0.5 to 2 h, and stirring and non-stirring conditions were compared. The Zn(NO<sub>3</sub>)<sub>2</sub> solution was refreshed every 10 min for all experiments.

To pre-deposit a seed layer, a Zn(OH)<sub>x</sub> compact film was electrodeposited at -1.2 V vs Ag/AgCl<sub>sat'd</sub> (-1 V vs Standard Hydrogen Electrode, SHE) from 50 mM Zn(NO<sub>3</sub>)<sub>2</sub> aqueous solution at room temperature, until a charge density of 30 mC cm<sup>-2</sup> was obtained (~23 min).

The film was converted into ZnO by annealing at 200 °C for 1 h [28, 29]. Other methods for seeding layer deposition that were explored produced larger diameter VNRs and their details can be found in the SI.

### 2.3 ZVNRs topography characterization

The ZVNRs topography was analyzed using Scanning Electron Microscopy (SEM) and image analysis. SEM was performed using the FEI NovaNanoSEM 450 and no conductive coating was necessary. Geometrical measurements were taken from top and cross-section SEM micrographs with ImageJ software. The average ZVNRs diameter ( $\bar{Q}_{\text{NR}}$ ), length, aperture angle (for truncated pyramidal ZVNRs), density ( $\rho_{\text{NR}}$ , number of ZVNRs in a given area) and surface-to-volume ratios were obtained by counting and measuring at least 200 ZVNRs from at least 5 different areas for each sample.

### 2.4 Photoelectron transport characterization

The electron transport measurements were performed using a dye-sensitized solar cell (DSC) configuration. The photo-anode was sensitized through a 12-h immersion in a 0.3 mM ethanoic solution of N3 dye (cis-Bis(isothiocyanato) bis(2,2'-bipyridyl-4,4'-dicarboxylato) ruthenium(II)) (Sigma-Aldrich). The counter-electrode was prepared by e-beam evaporation of a 40 nm/40 nm Ti/Pt film on a clean glass substrate. The photoanode and counter-electrode were clipped together to assemble the DSC, using a polydimethylsiloxane spacer. The cell was filled with an electrolyte of acetonitrile and ethylene carbonate in 2:1 volume ratio, 0.1 M LiI, 0.03 M I<sub>2</sub>, and 5% m v<sup>-1</sup> LiClO<sub>4</sub>. The DSCs were tested under a xenon lamp (USHIO UXL-75XE) with a power density of 100 mW cm<sup>-2</sup>, calibrated with a Newport Power Meter 1918-R. Electrochemical characterization of the devices was performed with the CHI 660C in a two-electrode configuration and CHI6005E electrochemical workstation software was used for recording the data.

The linear sweep voltammetry (LSV) was performed from 0.2 to -0.8 V. The open circuit voltage decay (OCVD) was measured by monitoring the open circuit voltage ( $V_{\text{OC}}$ ) of the DSC after switching from illuminated to dark operation. Electron lifetime  $\tau_n$  was calculated from the OCVD according to Eq. 3 [30]:

$$\tau = -\frac{k_B T}{n} \left( \frac{dV_{\text{OC}}}{dt} \right)^{-1} \quad (3)$$

The electrochemical impedance spectroscopy (EIS) was performed under illumination in the frequency range between 0.1 Hz and 100 kHz, setting the bias voltage at the  $V_{\text{OC}}$  of the device and the amplitude at 10 mV. EIS of

the photo-electrode was interpreted according to the most widely accepted model (Fig. S1). The equivalent circuit of a DSC is composed of electron diffusion through ZnO ( $R_d$ ) coupled to electron recombination reactions with the electrolyte ( $R_k$ ) in a transmission line model, in series to the charge transfer resistance at the ZnO/G interface ( $R_{\text{ZnO/G}}$ ) [31, 32]. More details on the impedance fitting can be found in SI [26].

## 3 Results and discussion

ZVNRs were electrodeposited on graphene under variable conditions. Table 1 details the electrodeposition parameters of stirring, seed layer, temperature ( $T$ ), and time ( $t$ ) studied for each sample and the morphology parameters of ZVNR density ( $\rho_{\text{NR}}$ ) and diameter ( $\bar{Q}_{\text{NR}}$ ) obtained from the analysis of SEM micrographs.

### 3.1 Effect of temperature and time

#### 3.1.1 Effect of temperature and time in the ZVNRs topography

The electrodeposition solution temperature ranging from 70 to 80 °C affects the topography of the ZVNRs, as shown in Fig. 2a–c'. At 70 °C, a sparse layer of randomly oriented ZVNR structures, while at 75 °C increased coverage and alignment is obtained, and the temperature at 80 °C causes even greater compactness and uniformity. The incomplete graphene coverage at 70 °C indicates that exclusion zones are formed due to concentration depletion that hinder further nucleation near existing growing nuclei [33]. As higher temperatures are applied, mass transfer is more efficient, leading to complete coverage of the graphene surface. A higher nucleation density causes the ZVNR average diameter to reduce from 475 nm at 70 °C, to 364 nm at 75 °C and 360 nm at 80 °C. At the same time, the NR density increases from  $1.8 \times 10^8$  cm<sup>-2</sup> for 70 °C, to  $3.4 \times 10^8$  cm<sup>-2</sup> for 75 °C and  $3.5 \times 10^8$  cm<sup>-2</sup> for 80 °C. Above 80 °C, the ZnO crystal growth rate in the lateral directions is faster, and the VNRs' walls eventually merge into grain boundaries to form a continuous ZnO layer rather than a ZVNRs carpet.

Extending the time of electrodeposition from 0.5 to 2 h results in an increase of ZVNRs dimensions, as reported previously on FTO [34]. The diameter increases from 360 to 790 nm, and the length increases from 0.9 mm to 3.1 mm, as observed in the SEM micrographs in Fig. 2c''–d''. The lateral growth of the ZVNR occurs at slower rate than the longitudinal, because of the higher energy configuration of the (0001) planes. However, the

slower growth in lateral directions still leads to the broadening of the ZVNR diameter at extended time, which results in the merging of the ZVNR into a mostly continuous film of ZnO.

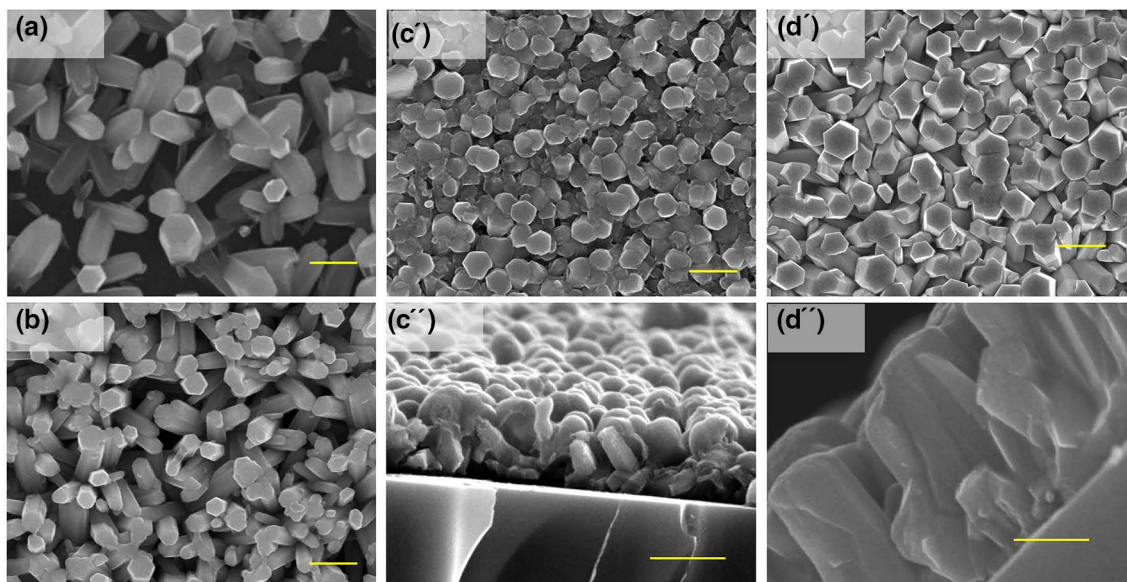
### 3.1.2 Effect of temperature and time in the ZVNR/G electrochemical characteristics

Figure 3a shows the potential-time ( $V-t$ ) curves for the electrodeposition of ZVNRs at the different temperatures. The potential range for the deposition is within the zone for ZnO formation in the Pourbaix diagram for the Zn/H<sub>2</sub>O system [35]. The curve corresponds to a mass transfer-controlled process showing four distinct regions [36, 37]. In stage I, a sudden increase of the potential is related to the double charge layer formation. Stage II is a short period of potential reduction, during which independent nuclei appear and grow on the surface of the graphene. This growth continues until

the formation of exclusion zones that virtually arrest further nucleation and a minimum potential is reached. Stage III is another region of potential increase which is more extended than stage I. During stage III, the two opposing processes of independent nuclei growth and nuclei overlapping take place simultaneously. This leads to electrode relative passivation due to gradual coverage of the conductive graphene, raising the overpotential required to maintain constant mass deposition. Finally, a plateau is reached in stage IV, in which the available graphene surface is either coated with ZnO or is an exclusion zone. During stage IV, steady growth occurs because a constant ionic concentration is maintained in the bulk of the electrolyte by refreshing the solution. Faster deposition rates in the [0001] direction lead to ZVNR formation [36, 37]. As a general trend, less overpotential is required at higher temperatures to maintain the galvanostatic conditions, due to the additional energy provided by the heat. The  $V-t$  curve obtained at 80 °C is absent of the potential

**Table 1** ZVNRs electrodeposition parameters, density ( $\rho_{NR}$ ) and diameter ( $\Phi_{NR}$ )

	Stir	Seed layer	$T$ (°C)	$t$ (h)	$\rho_{NR}$ ( $\times 10^8$ cm <sup>-2</sup> )	$\Phi_{NR}$ (nm)
1	✓	✗	70	0.5	1.8	475
2	✓	✗	75	0.5	3.4	364
3	✓	✗	80	0.5	3.5	360
4	✓	✗	80–75	2	1.9	790
5	✗	✗	80–75	2	5.5	487
6	✗	✓	80–75	2	43.4	134



**Fig. 2** SEM micrographs illustrating the effects of temperature and time on topography of ZVNRs grown on graphene grown by electrodeposition at **a** 70 °C and 0.5 h, **b** 75 °C and 0.5 h, **c**, **c'** 80 °C and 0.5 h, and **d**, **d'** 75–80 °C and 2 h. Scale bar 1 mm

drop seen in region II. This indicates that independent nuclei formation and nuclei overlapping occur almost instantaneously, and growth is not inhibited by exclusion zones at this temperature.

The heterostructure of ZVNR/G was used as the photoanode in a DSC. The transient photovoltage measurements in Fig. 3c show that as the ZVNR film becomes more compacted, the cells produce a higher photovoltage under illumination. The heterostructure grown at 70 °C yields a  $V_{oc}$  of 150 mV, at 75 °C it yields 190 mV, and at 80 °C it yields 300 mV. A slower  $V_{oc}$  decay indicates that the electron lifetime  $\tau$  is longer for the more compacted ZVNR films, as shown in Fig. 3c, d. The EIS of the devices grown at the different temperatures are described by the Nyquist plots in Fig. 3e, showing that as the graphene's surface becomes more densely coated, a larger  $R_k$  results, due to blocking

the contact between graphene and electrolyte. A more compacted film blocks the contact of the electrolyte with the graphene, increasing the  $R_k$  and slowing down the photoelectron loss kinetics, as observed in ZVNR/FTO photoanodes [34]. The formation of a more compact film also reduces the surface area and increases the imaginary impedance ( $Z''$ ) values, due to a reduction of the effective capacitance of the nanoporous film [38].

The desirable ZVNR morphology would be compacted at the bottom to prevent recombination losses from exposed graphene but with gaps between the ZVNRs at the top to provide higher interfacial area at the junction of the device. Therefore, for the remainder of the growth experiments, we used 80 °C during the first 10 min of growth and then cooled down the solution to 75 °C until the end of the ZVNR

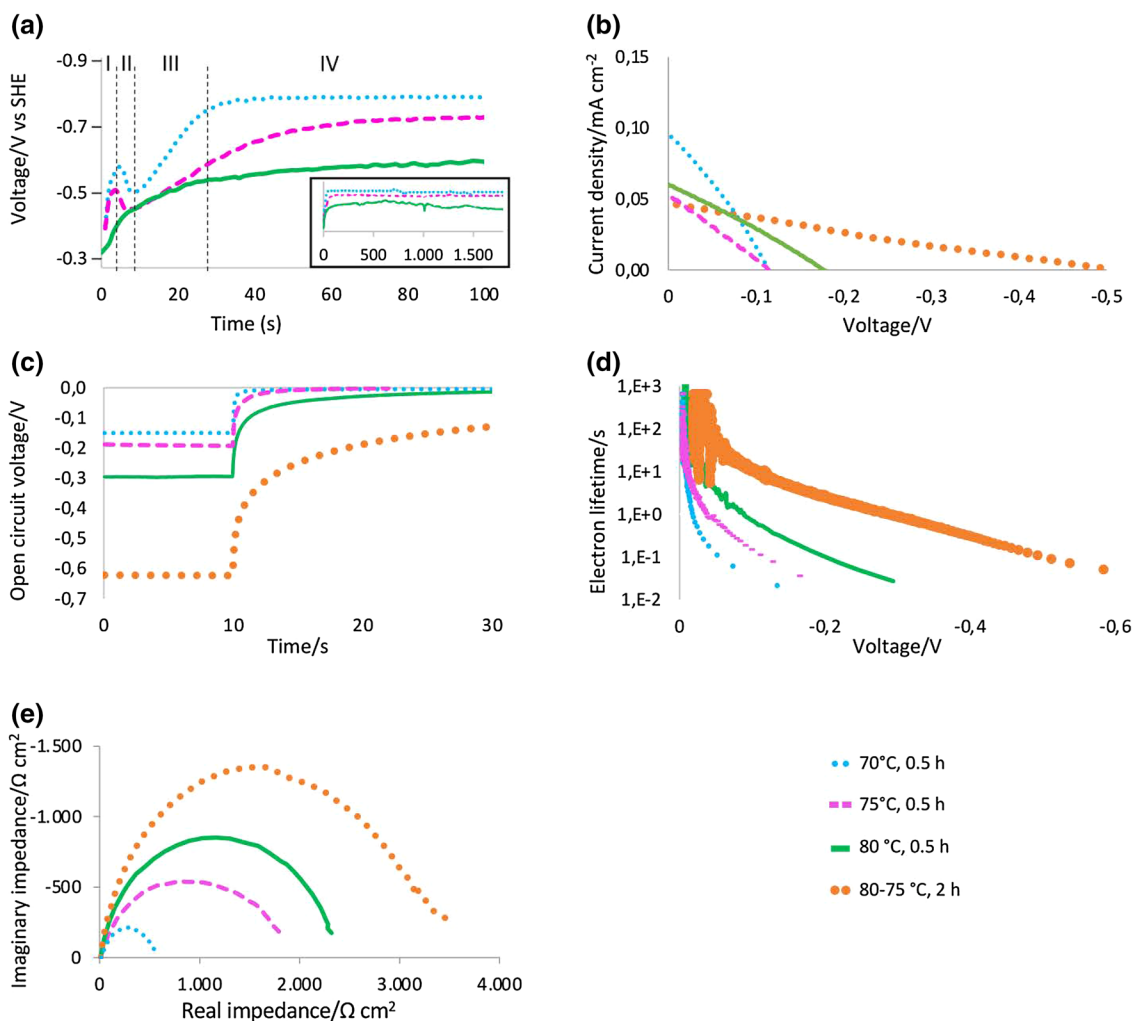


**Fig. 3** Effect of time and temperature in the electrochemical characteristics of ZVNR/G hybrid. **a** Applied potential as a function of time for ZVNR electrodeposition on graphene at constant current density of 0.4 mA cm<sup>-2</sup>. Photoelectrochemical response of DSC fabricated

with ZVNR/G sensitized with N3 dye in I<sup>-</sup>/I<sub>3</sub><sup>-</sup> under a Xe lamp with a power density of 100 mW cm<sup>-2</sup>. **b** Linear sweep voltammogram, **c**  $V_{oc}$  decay, **d** calculated electron lifetime  $\tau$  and **e** Nyquist plot of electrochemical impedance

growth. The term “80–75 °C” will be used to refer to this growth condition.

As time is extended from 0.5 h to 2 h, using the 80–75 °C conditions, the photoanode  $R_k$ ,  $V_{OC}$  and  $\tau$  increases because of its morphology (Fig. 3c–e), ascribed to the blocking of the graphene from the electrolyte, which prevented power loss events [34], and reduction of surface area [38]. The DSC  $V_{oc}$  doubles when the ZVNR were grown for 2 h instead of 30 min.

## 3.2 Effect of stirring

### 3.2.1 Effect of stirring in the ZVNRs topography

Even though the higher temperature and longer growth time increase the photovoltage of the electrode, the photocurrent remains low (Fig. 3b). Therefore, the stirring conditions during electrodeposition were varied to modify the mass transfer during ZVNR growth. When the VNRs grow in stirred conditions, straight rods grow as shown in Fig. 4a, while in unstirred conditions truncated pyramidal rods develop, shown in Fig. 4b. The length of the VNRs increase to 4.7 mm in unstirred conditions, compared to 3.1 mm for stirred conditions, while the diameter is reduced from 790 to 487 mm, which is expected to maintain constant mass deposition, i.e. constant current density. The truncated pyramidal shape and the increase in length are a result of increased  $Zn^{+}$  concentration gradient. Anisotropic growth occurs mostly along the  $c$ -direction of the crystal in unstirred conditions because  $Zn^{+}$  diffusion is significantly slower than  $OH^{-}$  generation. As the ratio of  $OH^{-}$  to  $Zn^{+}$  increases in the immediate vicinity of the electrode, most  $Zn^{+}$  ions are consumed at the tip of the rods, limiting lateral growth [19, 39]. In unstirred conditions, a threefold increase in VNR density is observed to yield  $5 \times 10^8$  VNRs  $cm^{-2}$ , compared to  $1.9 \times 10^8$  VNRs  $cm^{-2}$  in stirred conditions.

### 3.2.2 Effect of stirring in the ZVNR/G electrochemical characteristics

The  $V-t$  curves for the growth of the ZVNRs in unstirred and stirred conditions are compared in Fig. 5a. Similar growth mechanisms are observed under stirred and unstirred conditions, where 4 distinct growth stages take place, as analyzed previously [36, 37]. However, in unstirred conditions, nuclei formation in stage II occurs at faster rates. The reduced diffusion of ions along the graphene surface in unstirred conditions probably accelerates electro-crystallization, leading to faster achievement of the minimum potential, as exclusion zones form much faster. At the same time, nuclei growth in stage III occurs at much slower rates in unstirred compared to stirred conditions, and surface saturation takes 6 times longer. The slower mass transfer at the surface of the graphene when unstirred leads to slower deposition rate [40]. The potential plateau of stage IV has a similar value of  $\sim -0.7$  V vs SHE for unstirred and stirred conditions, given that the current density and temperature are identical. Therefore, the stirring conditions do not modify the thermodynamics of the system, but only the mass transfer kinetics.

The truncated pyramidal shape and higher density of the ZVNRs grown in unstirred conditions leads to a photocurrent twice as large as obtained for ZVNR grown under stirred conditions. This can be observed in Fig. 5b. However, the lower recombination resistance reduces the electron lifetime, which in turn lowers the  $V_{OC}$ , as shown in Fig. 5c–e. This result indicates that the increased space between ZVNRs causes electrolyte infiltration and short-circuiting between the redox mediator and the electrocatalytic graphene. The reduction of  $Z''$  values also indicate an increase of surface area [38]. Because non-stirred conditions resulted in larger surface area and photocurrent, with slight

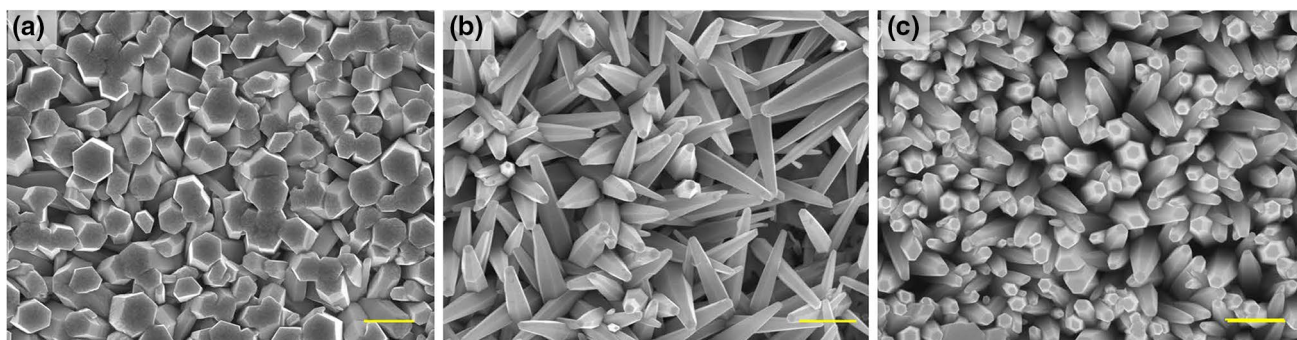


**Fig. 4** Effect of stirring and seed layer on ZVNR growth and photoanode performance. SEM micrographs of ZVNRs on graphene grown by electrodeposition at 80–75 °C conditions and 2 h **a** stirred, **b** without stirring, and **c** without stirring, using a seed layer

reduction of  $V_{OC}$  (Fig. 5c), these conditions were preferred for further experiments.

### 3.3 Effect of seed layer

#### 3.3.1 Effect of seed layer in the ZVNRs topography

The large domains in pristine CVD-graphene provide high mobility which is a desirable trait for transparent conductor application. However, the surface of CVD-graphene is very smooth, which results in lower nucleation rates and larger ZVNR diameter than those obtained in FTO [39], reduced graphene oxide (rGO) [41], and oxidized CVD-graphene

[21]. We deposited a seed layer to increase ZVNR nucleation density without reducing optoelectronic performance of the pristine CVD-graphene. Three methods were compared for depositing the seed layer: (i) spin coating of ZnO NPs [42, 43], (ii) spincoating of zinc acetate [44], and (iii) electro-deposition of  $Zn(OH)_x$  [28], all followed by thermal treatment. Methods (i), (ii) and (iii) result in ZVNRs diameters of 330, 274, and 135 nm respectively (Table S1), compared to the 487 nm obtained without seed layer. Electrodeposition of seed layer is the method that yields the smaller ZVNR diameter, with one order of magnitude increase in density, compared to those obtained without seed layer. Electrodeposition of seed layer is the method that yields the smaller ZVNR diameter, with one order of magnitude increase in density,

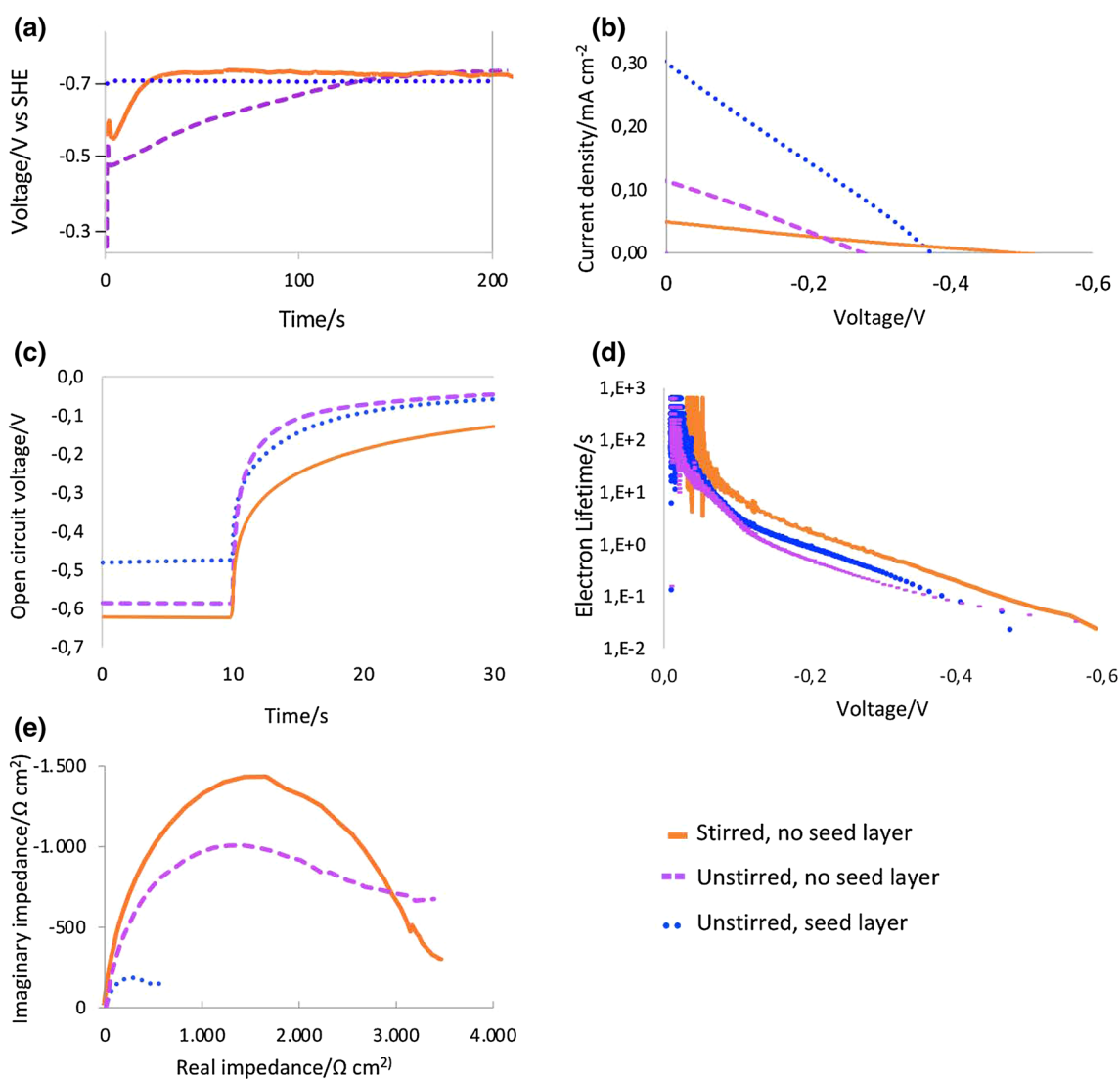


**Fig. 5** Effect of stirring and seed layer in the electrochemical characteristics of ZVNR/G hybrid. **a** Applied potential as a function of time for ZVNR electrodeposition on graphene at constant current density  $0.4 \text{ mA cm}^{-2}$ . Photoelectrochemical response of DSC fabricated

with ZVNR/G sensitized with N3 dye in  $I^-/I_3^-$  electrolyte under a Xe lamp with a power density of  $100 \text{ mW cm}^{-2}$  **b** linear sweep voltammogram, **c** Open circuit voltage decay (OCVD) **d** calculated electron lifetime and **e** Nyquist electrochemical impedance plot



as summarized in Table 1, and consistent with results on FTO [19]. Therefore, we focused on the electrodeposition as the method for depositing the seed layer. More details on the methods (i) and (ii) can be found in the SI.

### 3.3.2 Effect of seed layer in the ZVNR/G electrochemical characteristics

The presence of the seed layer on the graphene, modified the  $V-t$  curve of ZVNR growth, as shown in Fig. 5a. The  $V-t$  curve does not show the stages I, II, and III previously observed, but starts directly at the plateau potential of  $\sim -0.7$  V vs SHE. This indicates that the ZVNR electrodeposition on seed layer starts directly with growth stage, skipping the process of nucleation altogether. The plateau potential with and without seed layer is the same due to identical thermodynamic conditions, and similar to what was observed when comparing stirred and unstirred conditions.

Reducing the VNR diameter with the electrodeposited seed layer results in better light scattering, with a ten-fold increase in transmittance at 550 nm (Fig. S2). The larger junction area of smaller diameter ZVNRs, indicated by the smaller  $Z''$  [38], causes an overall three-fold increase in photocurrent generation and reduces the  $R_k$  (Fig. 5a, e). The photovoltage and electron lifetime remain high due to blocking of fast reactions at the graphene with the compact bottom layer of ZnO (Fig. 5c, d). The combination of higher photocurrent and open circuit voltage results in increased maximum power generation from  $8 \text{ mW cm}^{-2}$  (power conversion efficiency (PCE) of  $8 \times 10^{-3}\%$ ) without seed layer to  $63 \text{ mW cm}^{-2}$  (PCE of  $6.3 \times 10^{-2}\%$ ) with seed layer.

### 3.3.3 Optimization of seed layer deposition for reducing ZVNR diameter

The process of seed layer electrodeposition for ZVNR growth is detailed in Fig. 6a. At room temperature, the electrodeposition of a compact amorphous  $\text{Zn(OH)}_x$  layer takes place [28, 36]. Then, the  $\text{Zn(OH)}_x$  is decomposed into ZnO, a phase transition that occurs between 119 to 153 °C, we therefore performed the thermal treatment at 200 °C [28, 29]. The result is a compact film of ZnO NPs that control ZVNR growth and prevent shunt circuit contact with the transparent conductor. The seed layer deposition was optimized to further reduce the ZVNRs diameter. The initial conditions for the seed layer electrodeposition were 50 mM  $\text{Zn(NO}_3)_2$ ,  $-1$  V vs SHE, to attain  $30 \text{ mC cm}^{-2}$  and thermal treatment heating rate of  $5 \text{ }^\circ\text{C min}^{-1}$ , which yield 134 nm diameter VNRs (sample I). The increase of seed layer nucleation rate was attempted as detailed in Fig. 6b–c, by increasing the concentration of  $\text{Zn(NO}_3)_2$  to 200 mM (sample II) and the potential to  $-1.1$  V (sample III), but these did not reduce of the VNR diameters either (see Fig. 6b–c). The

total charge was also reduced to  $25 \text{ mC cm}^{-2}$  (sample IV) to limit  $\text{Zn(OH)}_x$  nuclei growth, but no reduction of the VNR diameter was observed either. As the variation of  $\text{Zn(OH)}_x$  electrodeposition conditions was not effective in reducing the VNR diameter, we opted for varying the thermal treatment instead in order to control the phase transition from  $\text{Zn(OH)}_x$  to ZnO (sample V). The heating rate of the material was accelerated by placing the sample directly in an oven at 200 °C. As a result, this faster nucleation rate of ZnO from  $\text{Zn(OH)}_x$  was effective in reducing the diameter to 83 nm. Therefore, we present the mechanism for seed layer formation and illustrate it in Fig. 6d. The deposition of  $\text{Zn(OH)}_x$  does not determine the grain size for the seed layer, as it is an amorphous and unstable film [28]. Instead, it is the phase transition itself, essentially the ZnO nucleation stage from  $\text{Zn(OH)}_x$ , which determines the size of the seed layer grains, and therefore, controls the ZVNR diameter. The electrodeposition of a  $\text{Zn(OH)}_x$  seed layer followed by thermal treatment may be preferred over other electrodeposition methods of ZnO seed layer, like pulsed electrodeposition [45], because electrodeposition of the former takes place at room temperature, while the latter only produces a compact and continuous film when performed using a solution heated above 60 °C [46]. The stability of graphene on the substrate may be compromised when applying several electrodeposition methods at high temperature, because of the increased energy of water molecules that may be introduced between graphene and glass, causing film peeling. Therefore, using a room temperature electrodeposition method may be advantageous for seed layer deposition in certain applications where a shorter time of exposure to high temperature electrodeposition bath is desired.

## 3.4 Discussion

We have studied the experimental correlations between the ZVNR/G electrodeposition parameters on the performances of the heterostructure as an electron transport layer and summarized them in Fig. 7. The ZVNR film can be made compact and dense by increasing both temperature (2–3) and time (4), to evenly cover the graphene surface and block recombination losses with the electrolyte. Charge collection of the photoanode was improved by blocking graphene, with a longer electron lifetime, larger photovoltage and higher recombination resistance. However, the reduction of surface area when the film becomes more compact limits the photocurrent generated because of hindered light scattering. Non-stirred conditions (5) promoted formation of longer truncated pyramidal ZVNRs and the use of a seed layer (6) reduced the ZVNR diameter. These two variables together resulted in a greater surface to volume ratio of ZVNR, for improved light scattering and higher photocurrent generation, while retaining high photovoltage, for a total ten-fold

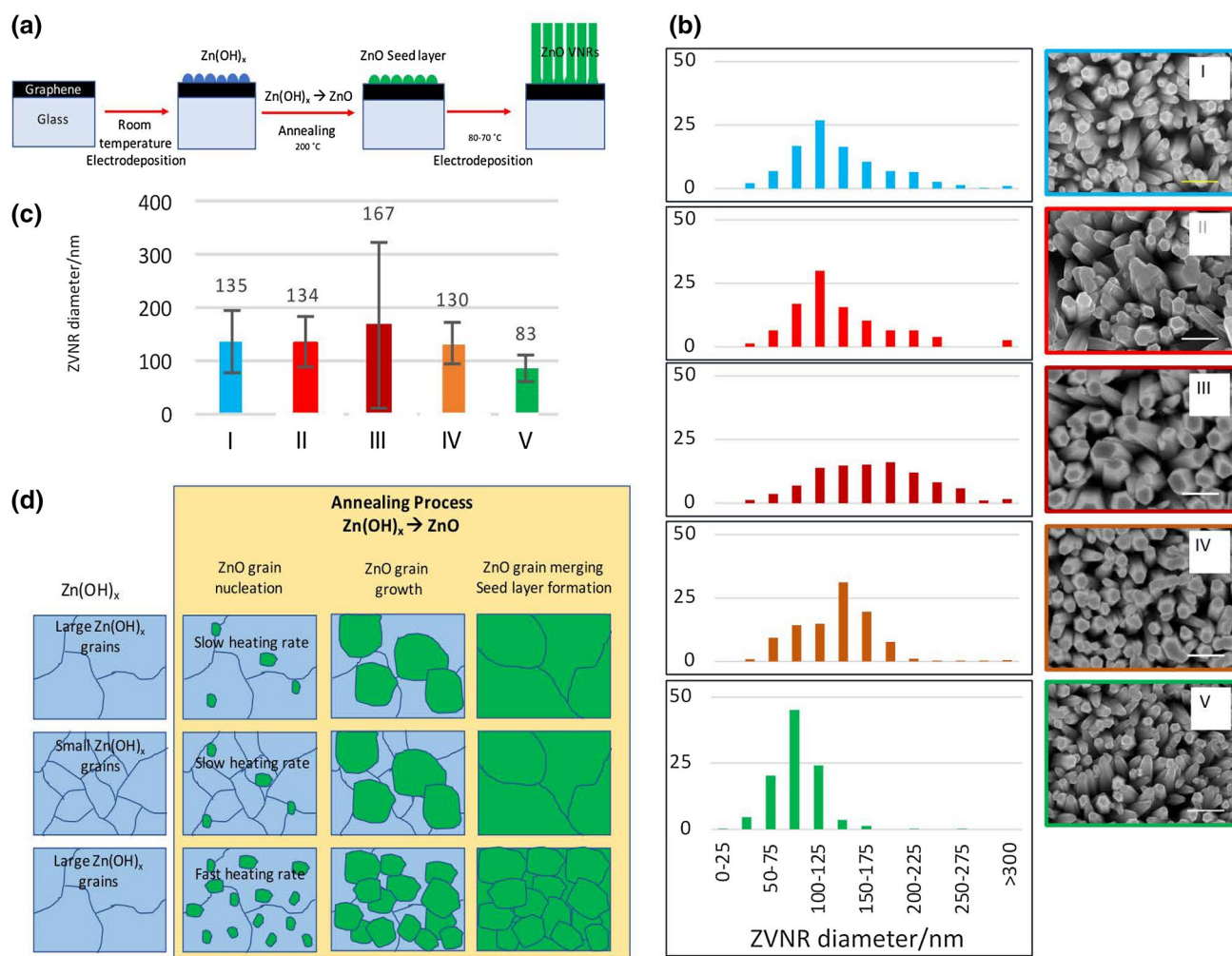


**Fig. 6** **a** Process of electrodeposition of seed layer and ZVNRs growth. **b** Effect of seed layer deposition on the ZVNR diameter distribution and SEM imaging. Seed layer deposition variables (I) control: 50 mM  $\text{Zn}(\text{NO}_3)_2$ , stirred,  $-1$  V vs SHE,  $30$   $\text{mC cm}^{-2}$ , slow

heating, (II) 200 mM  $\text{Zn}(\text{NO}_3)_2$ , (III)  $-1.1$  V vs SHE, (IV) 25  $\text{mC cm}^{-2}$ , (V) fast heating. **c** Average ZVNR diameter obtained for each variable. **d** Mechanism of seed layer formation which controls the diameter of the ZVNR.

improvement in power conversion. We explored the mechanism of seed layer electrodeposition to further reduce the ZVNR diameter. We found that the final diameter of the ZVNR is controlled by the seed layer process and depends on the phase transition from  $\text{Zn}(\text{OH})_x$  to ZnO during thermal treatment, rather than on the electrodeposition parameters.

## 4 Conclusions

Pristine CVD-graphene with large domains is an attractive option as a transparent conductor for photoelectrochemical cells due to its excellent optoelectronic properties. However, the preparation of graphene heterostructures to fabricate photoelectrochemical is challenging, as the smooth non-reactive surface of CVD-graphene delays nucleation,

making it difficult to grow very small nanocrystals like ZVNRs in situ. Very small nanocrystals are desirable to provide large junction area with the hole acceptor that ultimately determines the photocurrent generation. At the same time, the high catalytic activity of carbon results in electron recombination and power loss when it contacts the electrolyte or other hole acceptor material. Electrodeposition is a promising method for in situ growth of crystalline materials on graphene. We have studied the experimental correlations between the parameters of ZVNR electrodeposition on graphene and the corresponding performances of the heterostructure as a photo-electrode. Increasing temperature and time of ZVNR film growth increase compaction and density, resulting in an evenly covered graphene surface. This blocks recombination losses with the electrolyte, which improve the charge collection of the photoanode. However, the reduction

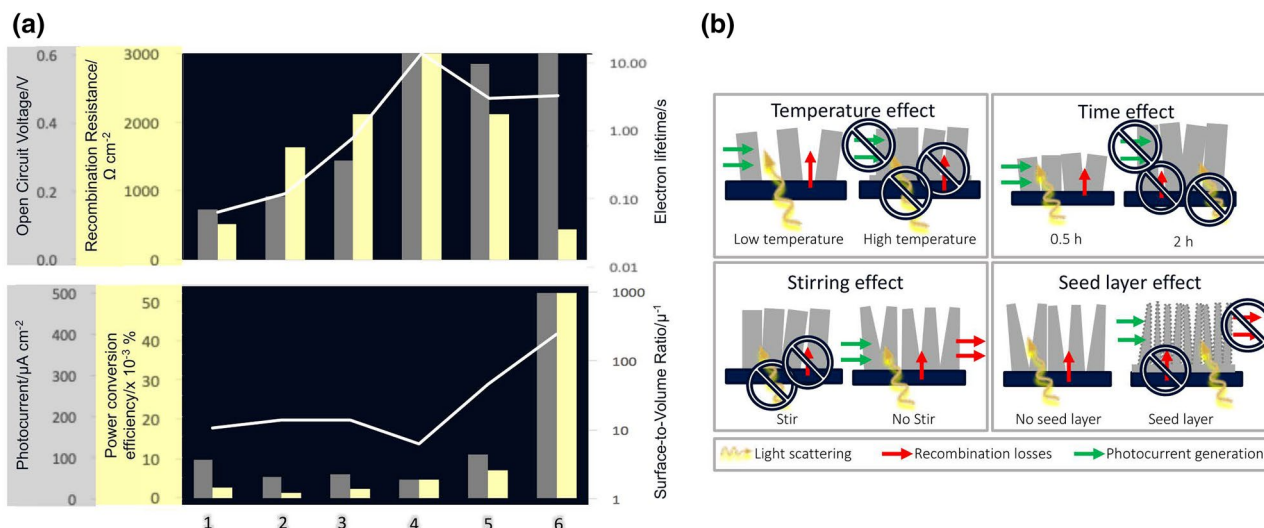


**Fig. 7** **a** Performance parameters for DSCs prepared with ZVNR/G photoanodes sensitized with N3 dye in  $\text{I}^-/\text{I}_3^-$  electrolyte under a Xe lamp with a power density of  $100 \text{ mW cm}^{-2}$ : (1) 70 °C, (2) 75 °C, and (3) 80 °C grown stirred for 30 min with and no seed layer, (4)

time increased to 1 h at 75–80 °C, (5) stirring was removed, (6) seed layer was pre-deposited. **b** Illustration of the effect that electrodeposition parameters have on the mechanisms of power generation (green arrows) and loss (red arrows) in ZVNR/G photoanode in a DSC

of surface area and hindered light scattering due to compacting of the film limits the photocurrent generated. Non-stirred conditions promoted formation of longer truncated pyramidal ZVNRs and the use of a seeding layer reduced the ZVNR diameter. These two variables together resulted in a greater surface to volume ratio of ZVNR, for improved light scattering and higher photocurrent generation, while retaining high photovoltage, for a total ten-fold improvement in power conversion. Controlling the seed layer deposition can reduce further the ZVNR diameter. The results of this study provide fundamental understanding for fabrication of hybrid ZVNR/G material by electrodeposition that can be used as an electron transport layer in a broad spectrum of photovoltaic devices, including cells sensitized with organic and metalorganic dyes, quantum dots, plasmonic nanoparticles, perovskites, and photosynthetic biomolecules.

**Supplementary Information** The online version contains supplementary material available at <https://doi.org/10.1007/s10800-021-01531-7>.

**Acknowledgements** A.M. acknowledges the financial support from W. Ruel Johnson Chair in Environmental Engineering. C.V. acknowledges Instituto Tecnológico de Costa Rica for the scholarship to pursue her Ph.D. studies at UC Riverside.

**Author contributions** CV was responsible for device design, materials fabrication, electrochemical measurements and original draft preparation; DP and AW collaborated in materials fabrication and electrochemical measurements; AW revised the manuscript; AM guided the revision of the manuscript and design of the study. All authors have read and agreed to the published version of the manuscript.

**Funding** The study was performed with the financial support from W. Ruel Johnson Chair in Environmental Engineering. Instituto

Tecnológico de Costa Rica supported the Ph.D. studies of C.V. in UC Riverside with a scholarship.

**Data availability** Data and materials used in the study are available upon request to the email [cchaves@itcr.ac.cr](mailto:cchaves@itcr.ac.cr).

## Compliance with ethical standards

**Conflict of interest** The authors declare that there is no conflict of interest or competing interests regarding the publication of this article.

## References



- Mathew S, Yella A, Gao P, Humphry-Baker R, Curchod BFE, Ashari-Astani N, Tavernelli I, Rothlisberger U, Nazeeruddin MK, Gratzel M (2014) Dye-sensitized solar cells with 13% efficiency achieved through the molecular engineering of porphyrin sensitizers. *Nat Chem* 6:242–247. <https://doi.org/10.1038/nchem.1861>
- Li T, Lee Y, Teng H (2012) High-performance quantum dot-sensitized solar cells based on sensitization with CuInS<sub>2</sub> quantum dots/CdS heterostructure. *Energy Environ Sci* 5:5315–5324. <https://doi.org/10.1039/C1EE02253A>
- Chandrasekhar PS, Komarala VK (2015) Effect of graphene and Au@SiO<sub>2</sub> core-shell nano-composite on photoelectrochemical performance of dye-sensitized solar cells based on N-doped titania nanotubes. *Rsc Adv* 5:84423–84431. <https://doi.org/10.1039/C5RA13799C>
- Kazim S, Nazeeruddin MK, Graetzel M, Ahmad S (2014) Perovskite as light harvester: a game changer in photovoltaics. *Angew Chem Int Ed* 53:2812–2824. <https://doi.org/10.1002/anie.201308719>
- Thakur UK, Askar AM, Kisslinger R, Wiltshire BD, Kar P, Shankar K (2017) Halide perovskite solar cells using monocrySTALLINE TiO<sub>2</sub> nanorod arrays as electron transport layers: impact

- of nanorod morphology. *Nanotechnology* 28:274001. <https://doi.org/10.1088/1361-6528/aa75ab>
6. Thavasi V, Lazarova T, Filipek S, Kolinski M, Querol E, Kumar A, Ramakrishna S, Padros E, Renugopalakrishnan V (2009) Study on the feasibility of bacteriorhodopsin as bio-photosensitizer in excitonic solar cell: a first report. *J Nanosci Nanotechnol* 9:1679–1687. <https://doi.org/10.1166/jnn.2009.si07>
  7. Mershin A, Matsumoto K, Kaiser L, Yu D, Vaughn M, Nazeeruddin MK, Bruce BD, Graetzel M, Zhang S (2012) Self-assembled photosystem-I biophotovoltaics on nanostructured TiO<sub>2</sub> and ZnO. *Sci Rep* 2:234. <https://doi.org/10.1038/srep00234>
  8. Badding MA, Fix NR, Orandle MS, Barger MW, Dunnick KM, Cummings KJ, Leonard SS (2016) Pulmonary toxicity of indium-oxide production facility particles in rats. *J Appl Toxicol* 36:618–626. <https://doi.org/10.1002/jat.3253>
  9. Polgreen L (2008) Congo's riches, looted by renegade troops. *The New York Times*. <https://www.nytimes.com/2008/11/16/world/africa/16congo.html>. Accessed 12 Aug 2015
  10. Commission S A E (2012) Final Rule-CONFLICT MINERALS. Securities and Exchange Commission. <https://www.sec.gov/rules/final/2012/34-67716.pdf>. S.A.E. Accessed 12 Aug 2015
  11. Xu XZ, Zhang ZH, Dong JC, Yi D, Niu JJ, Wu MH, Lin L, Yin RK, Li MQ, Zhou JY, Wang SX, Sun JL, Duan XJ, Gao P, Jiang Y, Wu XS, Peng HL, Ruoff RS, Liu ZF, Yu DP, Wang EG, Ding F, Liu KH (2017) Ultrafast epitaxial growth of metre-sized single-crystal graphene on industrial Cu foil. *Sci Bull* 62:1074–1080. <https://doi.org/10.1016/j.scib.2017.07.005>
  12. Zhang QF, Dandeneau CS, Zhou XY, Cao GZ (2009) ZnO nanostructures for dye-sensitized solar cells. *Adv Mater* 21:4087–4108. <https://doi.org/10.1002/adma.200803827>
  13. Kayes BM, Atwater HA, Lewis NS (2005) Comparison of the device physics principles of planar and radial p-n junction nanorod solar cells. *J Appl Phys* 97:114302. <https://doi.org/10.1063/1.1901835>
  14. Lewis NS (2007) Toward cost-effective solar energy use. *Science* 315:798–801. <https://doi.org/10.1126/science.1137014>
  15. Mu QH, Li YG, Zhang QH, Wang HZ (2011) Template-free formation of vertically oriented TiO<sub>2</sub> nanorods with uniform distribution for organics-sensing application. *J Hazard Mater* 188:363–368. <https://doi.org/10.1016/j.jhazmat.2011.01.125>
  16. Chandrasekhar PS, Dubey A, Qiao Q (2020) High efficiency perovskite solar cells using nitrogen-doped graphene/ZnO nanorod composite as an electron transport layer. *Sol Energy* 197:78–83. <https://doi.org/10.1016/j.solener.2019.12.062>
  17. Mamaghani KR, Naghib SM (2017) The effect of stirring rate on electrodeposition of nanocrystalline nickel coatings and their corrosion behaviors and mechanical characteristics. *Int J Electrochem Sci* 12:5023–5035. <https://doi.org/10.20964/2017.06.68>
  18. Izaki M, Omi T (1996) Transparent zinc oxide films prepared by electrochemical reaction. *Appl Phys Lett* 68:2439–2440. <https://doi.org/10.1063/1.116160>
  19. Khajavi MR, Blackwood DJ, Cabanero G, Tena-Zaera R (2012) New insight into growth mechanism of ZnO nanowires electrodeposited from nitrate-based solutions. *Electrochim Acta* 69:181–189. <https://doi.org/10.1016/j.electacta.2012.02.096>
  20. Elias J, Tena-Zaera R, Levy-Clement C (2007) Electrodeposition of ZnO nanowires with controlled dimensions for photovoltaic applications: role of buffer layer. *Thin Solid Films* 515:8553–8557. <https://doi.org/10.1016/j.tsf.2007.04.027>
  21. Rosas-Laverde NM, Pruna A, Busquets-Mataix D, Pullini D (2020) Graphene oxide-assisted morphology and structure of electrodeposited ZnO nanostructures. *Materials* 13:365. <https://doi.org/10.3390/ma13020365>
  22. Xu C, Lee JH, Lee JC, Kim BS, Hwang SW, Whang D (2011) Electrochemical growth of vertically aligned ZnO nanorod arrays on oxidized bi-layer graphene electrode. *CrystEngComm* 13:6036–6039. <https://doi.org/10.1039/C1CE05695F>
  23. Hambali NA, Yahaya H, Mahmood MR, Terasako T, Hashim AM (2014) Synthesis of zinc oxide nanostructures on graphene/glass substrate by electrochemical deposition: effects of current density and temperature. *Nanoscale Res Lett* 9:609. <https://doi.org/10.1186/1556-276X-9-609>
  24. Huang S, Wu PF, Yue HY et al (2019) ZnO nanosheet arrays/graphene foam: voltammetric determination of dopamine in the presence of ascorbic acid and uric acid. *J Mater Sci* 30:16510–16517. <https://doi.org/10.1007/s10854-019-02027-z>
  25. Gao LB, Ren WC, Xu HL, Jin L, Wang ZX, Ma T, Ma LP, Zhang ZY, Fu Q, Peng LM, Bao XH, Cheng HM (2012) Repeated growth and bubbling transfer of graphene with millimetre-size single-crystal grains using platinum. *Nat Commun* 3:699. <https://doi.org/10.1038/ncomms1702>
  26. Villarreal CC, Pirzada D, Wong A, Vi D, Pham T, Mulchandani A (2018) Characterisation of the heterojunction microstructure for electrodeposited vertical ZnO nanorods on CVD-graphene. *Mater Res Express* 5:085031. <https://doi.org/10.1088/2053-1591/aace06>
  27. Malekpour H, Ramnani P, Srinivasan S, Balasubramanian G, Nika DL, Mulchandani A, Lake R, Balandin AA (2016) Thermal conductivity of graphene with defects induced by electron beam irradiation. *Nanoscale* 8:14608–14616. <https://doi.org/10.1039/C6NR03470E>
  28. Zarebska K, Kwiatkowski M, Gniadek M, Skompska M (2013) Electrodeposition of Zn(OH)<sub>2</sub>, ZnO thin films and nanosheet-like Zn seed layers and influence of their morphology on the growth of ZnO nanorods. *Electrochim Acta* 98:255–262. <https://doi.org/10.1016/j.electacta.2013.03.051>
  29. Wang MS, Jiang LX, Kim EJ, Hahn SH (2015) Electronic structure and optical properties of Zn(OH)<sub>2</sub>: LDA+U calculations and intense yellow luminescence. *RSC Adv* 5:87496–87503. <https://doi.org/10.1039/C5RA17024A>
  30. Zaban A, Greenshtein M, Bisquert J (2003) Determination of the electron lifetime in nanocrystalline dye solar cells by open-circuit voltage decay measurements. *ChemPhysChem* 4:859–864. <https://doi.org/10.1002/cphc.200200615>
  31. Sarker S, Ahammad AJS, Seo HW, Kim DM (2014) Electrochemical impedance spectra of dye-sensitized solar cells: fundamentals and spreadsheet calculation. *Int J Photoenergy* 2014:851705. <https://doi.org/10.1155/2014/851705>
  32. Bisquert J (2002) Theory of the impedance of electron diffusion and recombination in a thin layer. *J Phys Chem B* 106:325–333. <https://doi.org/10.1021/jp011941g>
  33. Scharifker B, Hills G (1983) Theoretical and experimental studies of multiple nucleation. *Electrochim Acta* 28:879–889. [https://doi.org/10.1016/0013-4686\(83\)85163-9](https://doi.org/10.1016/0013-4686(83)85163-9)
  34. Son DY, Bae KH, Kim HS, Park NG (2015) Effects of seed layer on growth of ZnO nanorod and performance of perovskite solar cell. *J Phys Chem C* 119:10321–10328. <https://doi.org/10.1021/acs.jpcc.5b03276>
  35. Wiperman K, Schultze JW, Kessel R, Penninger J (1991) The inhibition of zinc corrosion by bisaminotriazole and other triazole derivatives. *Corros Sci* 32:205–230. [https://doi.org/10.1016/0010-938X\(91\)90044-P](https://doi.org/10.1016/0010-938X(91)90044-P)
  36. Nasirpour F (2017) Electrodeposition of nanostructured materials. *Springer, Cham* 62:1–325. <https://doi.org/10.1007/978-3-319-44920-3>
  37. Goux A, Pauporte T, Chivot LD (2005) Temperature effects on ZnO electrodeposition. *Electrochim Acta* 50:2239–2248. <https://doi.org/10.1016/j.electacta.2004.10.007>
  38. Dupuy L, Haller S, Rousset J, Donsanti F, Guillemoles FG, Lincot D, Decker (2010) Impedance measurements of nanoporosity in electrodeposited ZnO films for DSSC. *Electrochem Commun* 12:697–699. <https://doi.org/10.1016/j.elecom.2010.03.009>

39. Yin Z, Wu S, Zhou X, Huang X, Zhang Q, Boey F, Zhang H (2009) Electrochemical deposition of ZnO nanorods on transparent reduced graphene oxide electrodes for hybrid solar cells. *Small* 6:307–312. <https://doi.org/10.1002/sml.200901968>
40. Wan WT, Zhu LP, Hu L, Chen GF, Mi WB, Ye ZZ (2014) Investigation of morphology evolution of Cu-ZnO nanorod arrays and enhancement of ferromagnetism by codoping with N. *Phys Lett A* 378:2763–2767. <https://doi.org/10.1016/j.physleta.2014.07.040>
41. Tatiparti SSV, Ebrahimi F (2012) Potentiostatic versus galvanostatic electrodeposition of nanocrystalline Al-Mg alloy powders. *J Solid State Electrochem* 16:1255–1262. <https://doi.org/10.1007/s10008-011-1522-5>
42. Bera D, Qian L, Sabui S, Santra S, Holloway PH (2008) Photoluminescence of ZnO quantum dots produced by a sol-gel process. *Opt Mater* 30:1233–1239. <https://doi.org/10.1016/j.optmat.2007.06.001>
43. Greene LE, Law M, Goldberger J, Kim F, Johnson JC, Zhang YF, Saykally RJ, Yang PD (2003) Low-temperature wafer-scale production of ZnO nanowire arrays. *Angew Chem Int Ed Engl* 42:3031–3034. <https://doi.org/10.1002/anie.200351461>
44. Hsieh CT, Yang SY, Lin JY (2010) Electrochemical deposition and superhydrophobic behavior of ZnO nanorod arrays. *Thin Solid Films* 518:4884–4889. <https://doi.org/10.1016/j.tsf.2010.03.081>
45. Bhardwaj M, Balani K, Balasubramaniam R, Pandey S, Agarwal A (2011) Effect of current density and grain refining agents on pulsed electrodeposition of nanocrystalline nickel. *Surf Eng* 27(9):642–648. <https://doi.org/10.1179/026708410x12683118611185>
46. Salazar R, Lévy-Clément C, Ivanova V (2012) Galvanostatic deposition of ZnO thin films. *Electrochim Acta* 78:547–556. <https://doi.org/10.1016/j.electacta.2012.06.070>

**Publisher's Note** Springer Nature remains neutral with regard to jurisdictional claims in published maps and institutional affiliations.

## Authors and Affiliations

Claudia C. Villarreal<sup>1,3</sup>  · Danish Pirzada<sup>2</sup> · Annie Wong<sup>2</sup> · Ashok Mulchandani<sup>1,2,4</sup> 

<sup>1</sup> Department of Materials Science and Engineering, University of California Riverside, Riverside, CA 92521, USA

<sup>2</sup> Department of Chemical and Environmental Engineering, University of California Riverside, Riverside, CA 92521, USA

<sup>3</sup> Department of Materials Science and Engineering, Instituto Tecnológico de Costa Rica, Cartago 30101, Costa Rica

<sup>4</sup> Center for Environmental Research and Technology (CE-CERT), University of California Riverside, Riverside, CA 92507, USA